Enhancement of calcium copper titanium oxide photoelectrochemical performance using boron nitride nanosheets

Sara Kawrani, Amr A Nada, Maged F Bekheet, Madona Boulos, Roman Viter, Stéphanie Roualdes, Philippe Miele, David Cornu, Mikhael Bechelany

Enhancement of calcium copper titanium oxide photoelectrochemical performance using boron nitride nanosheets

Sara Kawrani [a,b], Amr A. Nada[a,f], Maged F. Bekheet [c], Madona Boulos [b], Roman Viter[d,e], Stéphanie Roualdes[a], Philippe Miele [a], David Cornu [a], Mikhael Bechelany [a]*

[a] Institut Européen des membranes, IEM, UMR-5635, Univ Montpellier, CNRS, ENSCM, Montpellier, France

[b] Laboratoire de Chimie Physique des matériaux, Université Libanaise, Liban

[c] Fachgebiet Keramische Werstoffe/Chair of Advanced Ceramic materials, Institut für Werkstoffwissenschaften und -technologien, Technische Universität Berlin, Hardenbergstraße 40, 10623, Berlin, Germany

[d] Institute of Atomic Physics and Spectroscopy, University of Latvia, 19 Raina Blvd., LV 1586, Riga, Latvia

[e] Sumy State University, Center for Collective Use of Scientific Equipment 31, Sanatornaya st., 40018, Sumy, Ukraine

[f] Dept. of Analysis and Evaluation, Egyptian Petroleum Research Institute, Cairo, Nasr City, P.B. 11727, Egypt

**Corresponding author: mikhael.bechelany@umontpellier.fr*

Abstract

Photoelectrochemical water splitting under visible light has attracted attention for renewable hydrogen production. Despite prevalent investigations, many challenges still hindered an efficient energy conversion, such as enhancing the reaction efficiency in visible light. Thus controlling the photoelectrode materials is an essential step in designing new materials for water splitting. $CaCu_3Ti_4O_{12}$ (CCTO) has received great attention as photocatalyst under visible light due to its combined band gap as result of the presence in its structure of TiO_2 active in UV light and CuO active under visible light. In this work, a cubic CCTO with different amount of exfoliated hexagonal boron nitride has been synthesized. The produced materials were fully characterized. Physico-chemical characterizations demonstrate that bore and nitrogen co-doped CCTO and causes an increase in grain

boundaries thickness, and thus leads to shift peaks in XRD and Raman spectra. UV-Vis diffuse reflectance spectroscopy showed a decrease of the bang gap value after adding boron nitride nanosheets into CCTO. The electrochemical performance and the resistivity of the obtained materials were performed using electrochemical impedance spectroscopy in dark and under visible light exposition. The onset potential recorded for CCTO with 3% of boron nitride nanosheets (Eg=2.9), is around 0.5V and the current generation is 16 times more than pure phase of CCTO. This work shows that CCTO with 3% of boron nitride nanosheets can be considered as an active photoelectrocatalyst under visible light irradiation for water splitting. Hydrogen production measurements shows that the rate of H_2 production reached arround 8.1 μmol/h under visible light after adding 3% of BN nanosheets to CCTO which presents 16 times increase in comparison with pure CCTO.

Key words:

- Water splitting
- Photoelectrochemical
- Visible light
- $CaCu_3Ti_4O_{12}$
- Hexagonal boron nitride nanosheets (h-BN)

Graphical abstract

In order to enhance the photoelectrochemical performance of CCTO and codoped with boron and nitrogen, different percentages of boron nitride nanosheets were used. The photoelectrocatalytic activity is enhanced by 16 times for CCTO with 3% of h-BN in comparison to pure phase of CCTO.

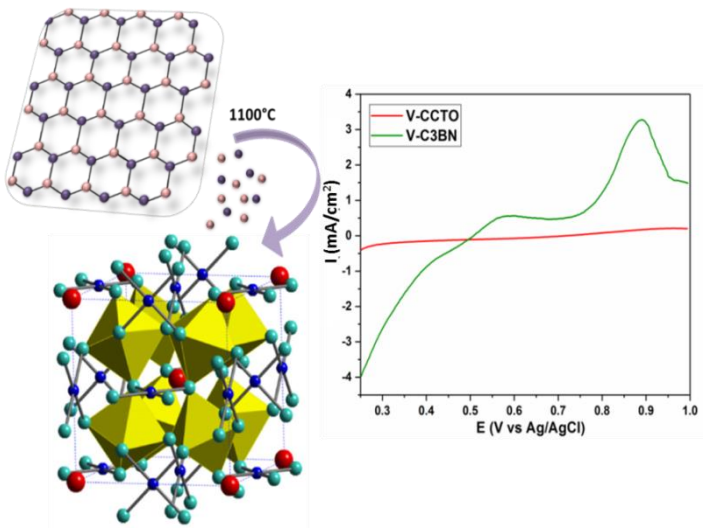

1. Introduction

Hydrogen production become a challenge as a source of renewable energy, and considerable efforts are currently undertaken to enriche its production. Hydrogen production can be carried out by several process such as chemical conversion of biomass and photoelectrochemical water splitting [1]–[3]. Chemical conversion of biomass are mainly classified into two categories, the thermochemical technology found on gasification and pyrolysis of raw materials such as coal, methanol, wood and gasoline to produce hydrogen [4] and the thermobiological technology. This process is based on photosynthetic activity of bacteria and green algae [5], [6]. Chemical conversion of biomass is widley used but it is limited by the reaction parameters control, such as temperature, heating / cooling rate, and the type of catalyst [7].

The Photoelectrochemical cell (PEC) is an advanced devices for water splitting technology . Several investigations focused to improve PEC cell efficiency for energy storage and hydrogen production. The main limit is that photoelectrocatalysts are active in UV light range which is only 4% from the received solar energy [8]. Oxygen evolution reaction (OER) and oxygen reduction reaction (ORR) are the principle electrochemical process that cover a wide range of electrochemistry conversion for energy storage and conversion devices [9]. The thermodynamic differences between the Two mechanisms reduce the probability to use one catalyst in ORR and OER in the same time [10].

Among the different materials used in PEC, noble metals such as platinum appears as very interested alternative and showed very good efficiency in acidic solution. However, its poor catalytic performance in alkaline solution, its high cost and its low abundance limit their applications [11]. Recent investigations focused on spinel materials as promissing candidates due to their chemical stability and specific optoelectronic properties. Spinel ferrites MFe_2O_4 ($M=Zn^{2+}$, Mg^{2+}, and Ca^{2+}) are widley investigated because their conduction and valence band levels that can potentielly be tuned via band hybridization with the M^{2+} states [12]. The aim of this combination is to bring the flat band gap potential closer to the hydrogen evolution potential with lowest onset voltage for water splitting. However these materials have not shown a significantly lower flat band potential and the onset potential is similar to that of Fe_2O_3 [13]. Metal oxides such as RuO_2 and MnO_2 play as well a significant role as catalysts of the oxygen evolution reaction (OER) and oxygen reduction reaction (ORR) in alkaline media. These oxides present an excellent behavior for OER mechanisms, but their high cost, poor stability, and their environmental issues limit their use [14]. Other oxides such as TiO_2 and WO_3 electrodes are easy to prepare and remerkably stable in electrochemical cell, but their wide band gap limit their activity under solar light for photoelectrochemical behavior [15], [16]. Studies were then conducted to mix semiconductors by doping or forming composites to reduce the band gap value able to photoinduced electrons under visible light exposition [17], [18]. However all these efforts did not succeed till now to create a highly active PEC cell.

ABO_3 perovskite oxides have gained attention recently due to their electrocatalytic behavior. In general they are composed from different oxides characterised by different band gap energies. This combination of band gap energy improves their photoelectrocatalytic efficiency. The structure of $CaCu_3Ti_4O_{12}$-CCTO (space group I*m3*) can be derived from an ideal cubic perovskite structure ABO_3 by superimposing a body centered ordering of Ca^{2+} and Cu^{2+} that share the A site, and Ti^{4+} is on B site. Due to the different ionic radius between Cu and Ca atoms, a tilting of TiO_6 octahedral planar appears [19]. This distortion forms a square planar oxide environment convenient to Jahn-Teller distorted Cu^{2+}. TiO_2 is an active photocatalyst in UV light and CuO is a good absorption component of visible light, thus merging properties in complex oxide $CaCu_3Ti_4O_{12}$ can enhance its properties under visible light exposition leading to photo-generate an electron-hole free movement in the ordered crystallographic sublattices of the complex oxide [20]. Recently, $CaCu_3Ti_4O_{12}$ was used as

photocatalyst for the decomposition of dye and pharmaceutical waste [21], [22]. It was found that the synthesis route used to prepare CCTO powder has a big influence on the properties of the obtained material.

$CaCu_3Ti_4O_{12}$ is established for the first as time as photo-electrocatalysis by Kushwaha *et al.* [22]. They conclude that under light irradiation, the current density increase to 0.97 mA/cm^2. In a second study, [23] they accomplished an electrochemical investigation and concluded that CCTO in octahedral shape shows a good performance for the decomposition of pollutants under visible light. They found that for crystallite size of 26 nm, CCTO synthesized using oxalate precursor route exhibit a bifunctional electrocatalytic activity (in OER and ORR range) with an onset potential of 0.83V. Investigations focused on that synthesis method leading to different powders structures [24] of CCTO and changing the electronic state of the material by doping result to a different electrocatalysts behavior. However the high recombination rate of the excited electron-hole limits the photocatalysis application of all oxides and specially CCTO. The separation between e-/h+ must be fast, and the recombination rate is decelerated by the high generation of current density [22]. Introducing material with different band gap is an efficient method to enhance the fast separation of electron-hole. One of the approaches that could be used to enhance this e-/h+ separation is the introducing of 2D materials in CCTO structures.

Among all two dimensional (2D), boron nitride nanosheets (h-BN) attracted attention because its outstanding properties [25]–[27]. BN is insulator with a wide ban gap (5.2 eV) depending on the synthesis method [28]. Boron nitride presents useful properties such as high chemical stability and thermal conductivity. Recent studies showed that hexagonal boron nitride nanosheets (h-BN) present a semiconducting and electronic transport similar to those of metals or metal oxides [29], [30].

In this paper, a new photoelectroactive CCTO/h-BN nanocomposite active under visible light has been prepared. Different percentages of BN nanosheets were added to CCTO powders (1, 3 and 6 wt% BN), and then pellets were prepared by a one-step conventional sintering at high temperature. The crystallinity and phase detection of the prepared samples were investigated by XRD and Raman techniques. Surface morphology and oxidation state of elements are detected by SEM and XPS respectively. Optical properties are studied using UV-Vis and photoluminescence spectroscopies. Finally we evaluated the electrochemical activity

(Cyclic and linear voltammetry measurements) and the resistivity (Impedance spectroscopy) of samples in Dark and under visible light irradiation in alkaline solution.

2. Experimental Section

2.1 Materials

Titanium (IV) Oxide (TiO_2- CAS Number: 13463-67-7, 99.5%), Potassium Hydroxide (KOH-CAS Number: 01900-20-08,≥85%) and gelatine from porcine skin(CAS Number: 9000-70-8) were purchased from Sigma Aldrich. Calcium Carbonate ($CaCO_3$-CAS Number: 471-34-1, 98%) and Copper (II) Oxide (CuO-CAS Number: 1317-38-0, 98%) were purchased from Alfa Aesar. BN nanosheets were prepared from commercial BN (Saint Gobain, 95%, 325 mesh). All chemicals were used without any further purification.

2.2. Exfoliation of BN

Boron nitride nanosheets were elaborated from commercial boron nitride powder with gelatin as reported elsewhere [31]. 20 g of porcine skin gelatine was dissolved in 80 mL of hot water (75 °C). After dissolution of gelatine, 1 g of BN was added to the solution. The mixture was kept overnight in an ultrasonic homogenizer at 50°C and it was sonicated for 3 hours at 65 % amplitude with pulse off/on 0.5 – 1 s. Exfoliated BN was collected from last precipitates by centrifugation at 6000 rpm for 30 minutes and the supernatant was collected to repeat the separation process for several times. The precipitates were dried at 80 °C for 48 hours and then calcined at 600 °C for 2 hours in air with a heating rate of 5 °C/min in order to obtain the pure exfoliated BN (Figure S1).

2.2 Preparation of $CaCu_3Ti_4O_{12}$ Pellets

First a stoichiometric mixture of the starting materials ($CaCO_3$, TiO_2 and CuO) was mixed by ball milling using Alumina (Al_2O_3) balls and a jar for 5h to minimize the powders size. Second the mixture was calcined at 900°C for 3h to obtain pure CCTO powders with a pseudo-spherical shape of powders. Then calcined powders were pressed into pellets (d=10 mm, e=1-2 mm) by uniaxial hydraulic compression at 3.5T. In a final step, CCTO pellet was sintered in air at 1100°C for 3h.

2.4 Preparation of CCTO (1%BN), CCTO (3%BN) and CCTO (6%BN)

$CaCu_3Ti_4O_{12}$/ x%h-BN ceramics (x% =1, 3 and 6) were prepared using solid state reaction method**.** The calcined powders were mixed and ground with different percentages of h-BN nanosheets and pressed into pellets with 10 mm of diameter and 1-2 mm in thickness by a uniaxial hydraulic compression at 3.5T. Finally these pellets were sintered in air at 1100°C for 3h. The obtained pellets are labeled CCTO, C1BN, C3BN and C6BN corresponding to pure phase of $CaCu_3Ti_4O_{12}$, CCTO (1%BN), CCTO (3%BN) and CCTO (6%BN) respectively.

2.5 Characterizations of pellets

The crystalline phase of the obtained pellets was analyzed by X-ray diffraction (XRD), using a PANAlytical Xpert-PRO diffractometer equipped with an Xcelerator detector using Ni-filtered Cu-radiation with wavelength of 1.54 A. The scan step size of all prepared pellets was fixed at 0.0167°/step and the time per step was 0.55 sec/step. Rietveld refinement was performed using the FULLPROF program [32]. The morphology of all ceramics was studied via scanning electron microscopy (SEM), where images were taken with a Hitachi S4800, Japan. Elemental mapping were performed with a Zeiss EVO HD15 microscope coupled with an Oxford X-MaxN EDX detector. Raman spectra were measured by the dispersive Raman spectroscopy (Horiba XploRA), λ=659 nm at a power of 20 W with a continuous mode time of 10 seconds, snapshot time of 7 seconds (number of accumulations set to 30 times) as acquisition conditions, and using an objective lens of 100x. In order to investigate the oxidation state of elements in pellets, X-ray photoelectron spectroscopy (XPS) was performed using XPS: monochromatic X-ray source: Al-Kalpha, 1486.6 eV - Resolution FWHM 0.45 eV.

The band gab of pellets was measuring from UV–vis spectra. These spectra were measured by a UV–vis spectrophotometer (Jasco model V-570) equipped with a diffuse reflectance (DR) attachment (Shimadzu IRS-2200). Room temperature photoluminescence (PL) was measured in the range of 350–900 nm. After excitement with a nitrogen Nd:YAG laser (266 nm, 10 mW, 1 kHz), PL was recorded with an optical fiber spectrometer (Ocean Optics usb2000).

2.6 Electrochemical measurements

Electrochemical measurements for ORR and OER were carried out in a three- electrode system using 1 M KOH as the electrolyte in dark and under visible light exposition using 150 W linear halogen lamp (the visible light source is in the range of 420-600 nm). CCTO and h-

BN (x%)/CCTO pellets with a diameter of 10 mm was used as working electrode, Ag/AgCl as reference electrode and platinum wire as counter electrode. Electrochemical Impedance spectroscopy measurements in dark and under visible light irradiation were performed at room temperature in the frequency range of 0.01Hz to 10^6 kHz with voltage bias of 20 mV amplitude. The distance between the lamp and the Quartz window was maintained at 10 cm. Hydrogen generation measurements were performed in which gas samples has been collected using a syringe every 30 minutes, and had been measured using gas chromatography (Clarus-400, PerkinElmer, TCD (2mx1mm), He carrier).

Quantum Efficiency (QE) was calculated in order to present the catalytic results. QE was defined by Equation (1)

$$QE=\frac{2.N(H2)}{N\ (\text{absorbed photons})} \quad (1)$$

where $N(H_2)$ and Nabsorbed photons are number of hydrogen molecules and absorbed photons, respectively.

The number of hydrogen molecules can be calculated as:

$$N\ (H_2) = \mu(mol)*6.02*10^{23} \quad (2)$$

The number of absorbed photons was estimated in the following way:

$$N\ (\text{absorbed photons}) = \sum_{400nm}^{800nm} \eta(\lambda) * S * (1 - e^{-\alpha(\lambda)})/h\nu/e \quad (3)$$

Where λ, η(λ), S, α(λ), hν, e are wavelength of incident light, power density of light with wavelength λ (W/m^2), area of the reactor, absorption coefficient, photon energy in eV and electron charge, respectively.

In fact, rough evaluations of the scattered light will allow assuming that the scattered light intensity will depend on nanofiber concentration, molar mass and refractive index as reported elsewhere

$$I \sim \frac{n_0^2 * C * M * \frac{dn}{dC}}{\lambda^4} \quad (4)$$

Where I, n0, C, M, dn/dC and λ are the scattered intensity, the refractive index of the solvent, the concentration of the ceramics, the average molecular weight of the ceramics, the change of the refractive index after adding of the ceramics and the light wavelength, respectively.

The estimated values were: 0.092% for CCTO and 0.71% for C3BN (CCTO with 3%BN).'

Results and discussions

Pellets from pure phase of CCTO and with different amounts of hexagonal boron nitride (x=1, 3 and 6%) were synthesized using mecanosynthesis method, followed by sintering step at 1100°C for 3h. The crystallinity and morphology of pellets are characterized by XRD, SEM, XPS and Raman. The optical properties were investigated using UV-Vis and

photoluminescence measurements. Finally, in order to study the performance of the obtained materials under visible light and their resistivity, electrochemical measurements (cyclic and linear voltammetry) and impedance spectroscopy were performed in a system using three electrodes in 1M of KOH solution.

Physico-chemical characterization

The XRD data of the samples sintered at 1100°C for 3h under air are shown in Figure 1. The reflections of XRD patterns of examined materials can be indexed to the cubic structure of $CaCu_3Ti_4O_{12}$ (space group *Im*-3) as a main phase and monoclinic CuO (space group *C*2/*c*) as minor phase. Rietveld refinement (Figure 2) of XRD patterns revealed that the grains of the sintered samples are preferentially grown along the [422] direction. The lattice parameter *a* of $CaCu_3Ti_4O_{12}$ phase in CCTO sample found to be 7.38958 (8), which is in good agreement with previously reported value for pure $CaCu_3Ti_4O_{12}$ [33]. On the other hand, the addition of BN resulted in a slight increase in the lattice parameter of $CaCu_3Ti_4O_{12}$ phase (a = 7.39375 (7), 7.39343 (5) and 7.39535 (6)) Å for C1BN, C3BN and C6BN sample, respectively). This increase in the lattice parameter can be explained by the incorporation of B or N in the lattice of $CaCu_3Ti_4O_{12}$, as confirmed by XPS results later. The change in the cation stoichiometry of $CaCu_3Ti_4O_{12}$ could be another reason for this increase as the partial reduction of Cu^{2+} or Ti^{4+} cations for charge compensation lead to the expansion of CCTO phase. As it can be seen in Figure 1, the intensities of XRD reflections corresponding to CuO phase are drastically changed with the addition of h-BN, indicating the change in the amount of CuO phase on the surface of sintered samples. The intensities ratio of the (11-1) reflection for CuO and (211) reflection for $CaCu_3Ti_4O_{12}$, which does not suffer from preferred orientation, increases with h-BN nanosheets amount. However, it was difficult to quantify precisely the amount of CuO phase in the samples by Rietveld refinement due to the strong preferred orientations observed for $CaCu_3Ti_4O_{12}$ phase. Therefore, Rietveld refinement was also performed on the diffraction data of powdered samples obtained by grinding the sintered pellets in order to reduce the influence of preferred orientations. Figure 2 a-d show the observed, calculated and the difference profile for the final cycle of the structure refinement. The final structure parameters of four samples and Rietveld R-factors are given in Table 1. As shown in Figure 2, the preferred orientation and the intensity of XRD reflections corresponding to CuO phase are drastically reduced in the powdered samples, suggesting that most of CuO phase was present on the surface of the pellets. Surprisingly, the weight fractions of CuO phase were found to be

very close in the four powdered samples (Table 1). This result suggests that the total amount of CuO phase, which was already present in the CCTO sample, does not change with the addition of BN but diffuses from the grain interiors to the surface during sintering process. Moreover, in contrast to $CaCu_3Ti_4O_{12}$ phase, the lattice parameter and unit cell volumes of CuO phase don't remarkably change with the addition of BN nanosheets, indicating that the CuO lattice has not been affected by BN such as in case of $CaCu_3Ti_4O_{12}$.

Moreover, no characteristic XRD reflections corresponding to any of crystalline BN phase are observed in the XRD patterns of all samples. In contrast, XPS analysis revealed the presence of elemental boron and nitrogen in the sintered samples as it will be showed later. These results could be due to the h-BN phase is present in a very small amount to be detected by XRD measurements in the presence of highly crystalline $CaCu_3Ti_4O_{12}$ and CuO phases or the incorporation of B or N in the lattice of $CaCu_3Ti_4O_{12}$ and CuO phases due to the oxidation of boron nitride nanosheets at high temperature under air, as confirmed by XPS results.

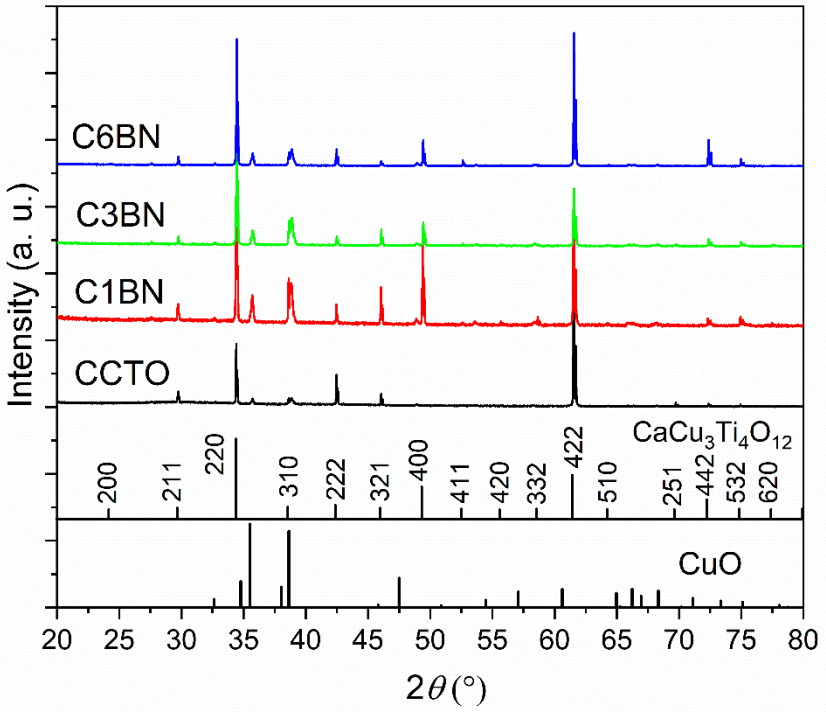

Figure 1 : X-ray diffraction patterns of CCTO, C1BN, C3BN and C6BN ceramics sintered at 1100°C/3h.

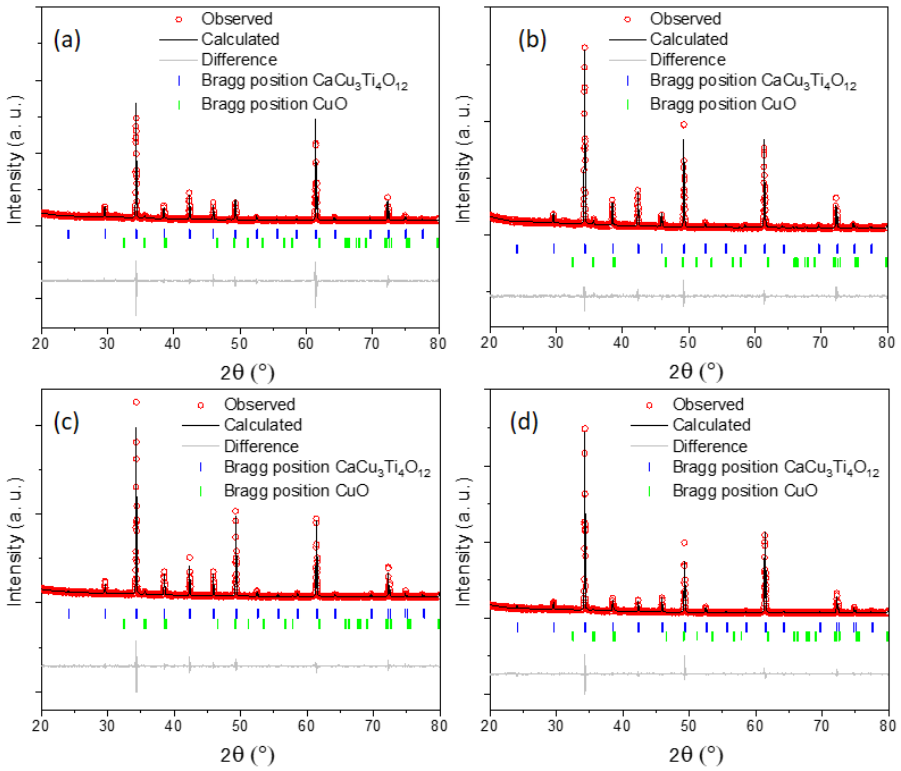

Figure 2 : Rietveld Refinement of (a) CCTO, (b) C1BN, (c) C3BN, and (d) C6BN ceramics

Table 1: A summary of structural parameters extracted from powder XRD patterns by Rietveld refinement of CCTO, C1BN, C3BN, C6BN samples showing weight fraction wt. [%], lattice parameters *a* , *b* and *c* [Å], unit cell volume *V* [Å^3].

Phase	**Parameters**	**CCTO**	**C1BN**	**C3BN**	**C6BN**
$CaCu_3Ti_4O_{12}$	*a* (Å)	7.38958(8)	7.39375(7)	7.39343(5)	7.39535(6)
	V (Å^3)	403.52(1)	404.20(1)	404.15(1)	404.46(1)
	wt.(%)	98.8(0.9)	97.4(0.8)	97.1(0.9)	98.0(0.7)
CuO	*a* (Å)	4.6968(5)	4.6981(8)	4.6914(2)	4.6952(2)
	b (Å)	3.4193(3)	3.4221(3)	3.4240(1)	3.4239(1)
	c (Å)	5.1323(5)	5.1291(9)	5.1356(2)	5.1342(3)
	β (°)	99.30(1)	99.37(1)	99.35(2)	99.32(3)
	V (Å^3)	81.34(1)	81.36(2)	81.40(1)	81.45(1)
	wt.(%)	2.2(0.2)	2.6(0.3)	2.9(0.3)	2.0(0.2)
Reliability factors (%)	R_p	5.87	4.77	4.81	4.83
	R_{wp}	9.30	6.31	6.50	6.56
	R_{exp}	4.39	4.57	4.48	4.37
	X^2	4.50	1.90	2.11	2.25

The morphology and microstructure of the obtained ceramics were examined using SEM. Figure 3 shows the microstructural evolution of CCTO ceramics sintered at 1100°C for 3h under air after adding 1,3 and 6% of BN nanosheets. The presence of two regions is noticed in all the ceramics : the grain region and the grain boundaries region. The grain diameter and the thickness of the grain boundaries region are highly influenced by the addition of h-BN nanosheets. For the pure CCTO ceramic the grain size, obtained using ImajJ, Java-based image processing software, is 104.9 $\pm$0.5 µm. The grain sizes decreases to 101.1$\pm$0.3 µm, 63.8$\pm$0.3 µm and 64.4$\pm$0.5 µm for C1BN, C3BN and C6BN respectively.

It is well known that during the sintering process, the mass diffusion of ions takes place through the grain boundaries region. The added elements (dopant, nanosheets or nanofillers) can melt or react with the present major phase and form a eutectic liquid phase. In ceramics, the liquid phase is mainly present between the grains making it easier for the ions to diffuse. The temperature of eutectic liquid phase for the system CuO-TiO_2 is between 900 and 950°C, depending from CuO/TiO_2 ratio in which CuO phase transforms into liquid during the sintering treatment [34]. XRD studies showed that adding boron nitride nanosheets to CCTO leads to the diffusion of CuO from the grain interiors to the surface during sintering process. The amount of CuO increases with the increase of the percentage of h-BN nanosheets. The presence of the CuO phase will create a liquid phase during the sintering process that increases the thickness of the grain boundaries region. From the SEM images, we can notice an increase in the grain boundaries thickness and a decrease in the grain size with the addition of h-BN nanosheets. The thickness of the grain boundaries region increases with the increase in the percentage of h-BN nanosheets. This is mainly due to the increase in the amount of CuO phase after adding the BN nanosheets.

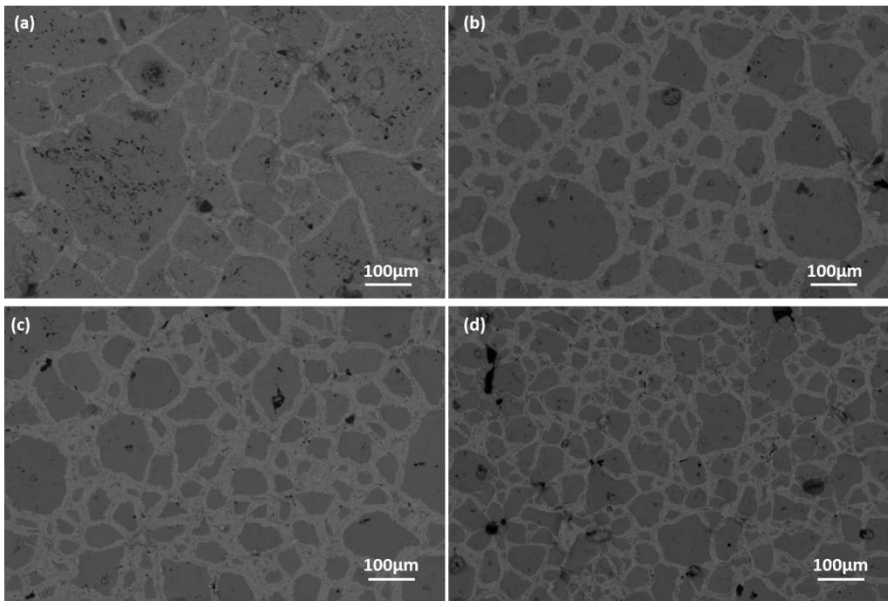

Figure 3 : Scanning electron micrographs of the pellets (a) CCTO, (b) C1BN, (c) C3BN, (d) C6BN sintered at 1100°C/3h

Figure 4 shows the SEM/EDX mapping images of CCTO (Figure 4a), C1BN (Figure 4b) and C3BN (Figure 4c). It confirms the presence of all major elements (Ca, Ti, Cu and O). It is clear that adding boron nitride nanosheets leads to increase the Copper ratio at grain boundaries. Thus confirms that adding boron nitride nanosheets enhances the formation of a liquid phase originated from the eutectic phase TiO_2-CuO. Using SEM/EDX mapping could not detect the dispersion of h-BN nanosheets because B and N are a light element and EDX is not sensetive to these elements.

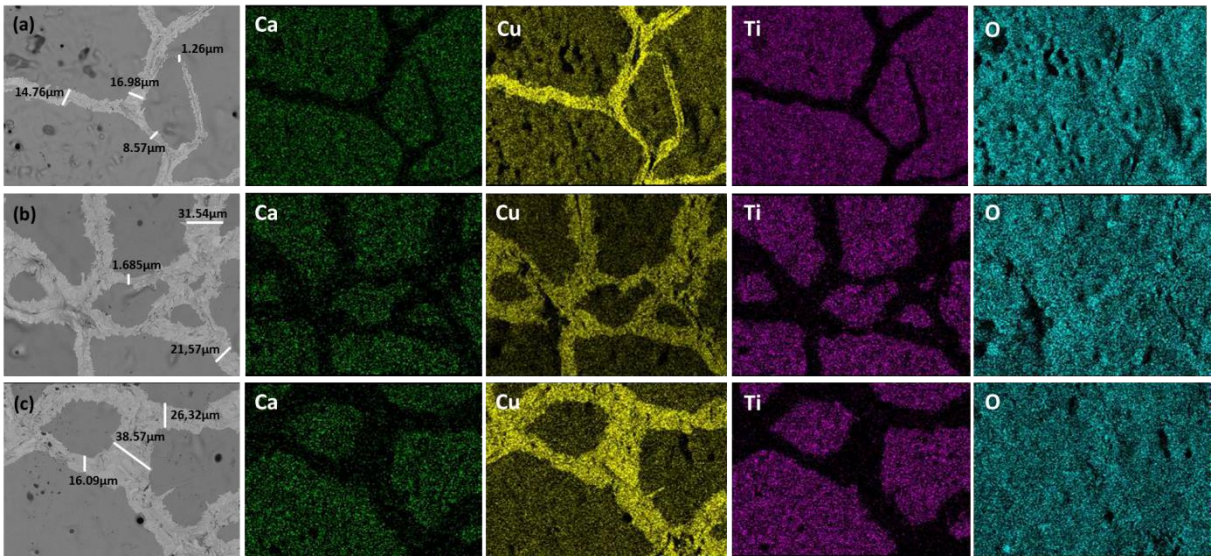

Figure 4 : SEM/EDX mapping of (a) CCTO, (b) C1BN and (c) C3BN ceramics.

High resolution XPS analysis of pure and composite CCTO has been carried out to know the oxidation states of the constituent elements and to confirm the presence of oxygen vacancies responsible of a good electrochemical behavior. The XPS scan shows the presence of Ti 2p, Cu 2p, and O 1s at their corresponding binding energies in pure CCTO and the presence of Ti 2p, Cu 2p, O 1s, B 1s and N 1s in CCTO-BN composites (Figure 5). Figure 5a shows XPS data of oxygen atoms for CCTO composites, it indicates an increase in the defect of $CaCu_3Ti_4O_{12}$ lattice with the increase of h-BN percentage in CCTO matrix. As shown in Figure 5a, O1s spectrum can be fitted with four peaks at about 528.97, 530.55, 531.92, and 533.22 eV corresponding to the lattice oxygen Cu^{2+}-O_L, Cu^{1+}-O_L, oxygen vacancv O_V and adsorbed oxygen (i.e. adsorbed H_2O), respectively [35]–[37]. As observed in this figures, the area ratio of O_V to O_L peak increases in the composite samples if compared with than that of CCTO. The ratio of O_V/O_L increases from 0.6 for CCTO to 1.2 and 1.1 for C1BN and C3BN, respectively, suggesting that increasing the amount of boron nitride nanosheets increase the surface defects of the material. A slight shift of peaks to a lower binding energy is observed for $Ti^{4+}$and Cu^{2+} (figure 5b and 5c). Shifting of peaks are maybe due to the segregation of Cu on grain boundaries, in which the segragation increases the surface stress and lead to produce an effective pressure to raise the force constants [38], [39]. In addition to that, this shifting might be due to the partial reduction of Ti^{4+} and Cu^{2+} with the creation of oxygen vacancies and the insertion of B and N in TiO lattice. For instance, the ratio of Cu^{+1} (obseved at about 931.96 eV) to Cu^{2+} (obseved at about 933.25, 934.3 and 935.46 eV) [40] increases from 0.11 for CCTO to 0.17 and 0.14 for C1BN and C3BN, respectively. Moreover, the oxygen vacancy arises from presence of Ti^{3+} can also be confirmed from peak observed at higher binding energy (~458.13 eV) in the Ti $2p_{3/2}$ spectra of the three samples (Figure 5c) [37]. The area of this peak for C1BN and C3BN samples is larger than that for CCTO sample. On the other hand, the B1s and N 1s XPS spectra (Figure 5d and e), are well fitted with four different peaks. The peaks of boron and nitrongen observed at about 191.1 and 398.49 eV, rspectively, can be assigned to *h*-BN [41]. The additional three peaks in both specta suggest that BN nanosheets may be partially decomposed, oxidized and incorporated in CCTO lattice, which is in good agreement with XRD results.

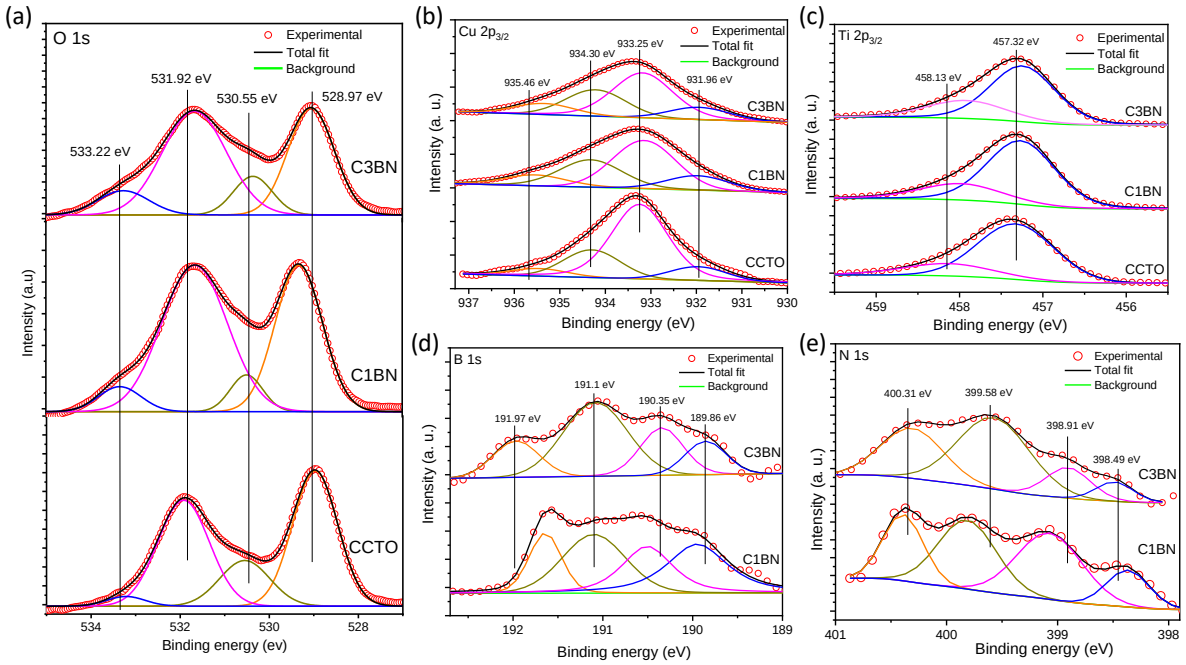

Figure 5 : High resolution XPS Spectra of (a) O 1s, (b) Cu $2p_{3/2}$, (c) Ti $2p_{3/2}$, (d) B 1s, and (e) N 1s spectra, of CCTO, C1BN, and C3BN.

CCTO and h-BN/CCTO were further studied by confocal Raman analysis. In order to confirm the crystalline quality and the presence of the different phases in the obtained materials, Raman spectra were recorded between 50 and 600cm^{-1}. Figure 6i shows the Raman spectra of the grain and grain boundaries regions for the ceramics CCTO, C1BN, C3BN and C6BN. In general, the position of the Raman modes frequencies in metal oxides is affected by the effective charge, the asymmetry, the bond length of the participating atoms and the vibrational modes of atoms. Three main modes close to 445, 506 and 570 cm^{-1} are essential to determine CCTO [42]. All mentioned modes (P7, 8 and 9) are related to TiO_6 clusters. P7 and P8 modes appear in all samples and in both regions corresponding to wavelenght near to 445cm^{-1} and 506cm^{-1} respectively related to TiO_6 clusters in the Ag symmetries. These two modes are slightly shifted to an emission of high energy for 1, 3 and 6% BN samples resulted from a stress generated in c axix produced by B^{3+} and N^{3-} ions introduced in TiO lattice. The third mode P9 close to 570 cm^{-1} (Fg symmetrie) is an antistretching mode Ti-O-Ti for the TiO_6 octahedras and appears only for CCTO, C3BN and C6BN samples, which mean that the amount of polarization strenght has been influenced by doping because the Raman scattering intensity is determined by amount of polarization strenght [43]. Figure 6ii shows Raman spectra on grain boundaries; as reported grain boundaries are dominated by CuO.

For all samples, TiO_2 phase appears. P7 and P8 modes characteristic of CCTO phases are present in different intensity for C1BNand C6BN.

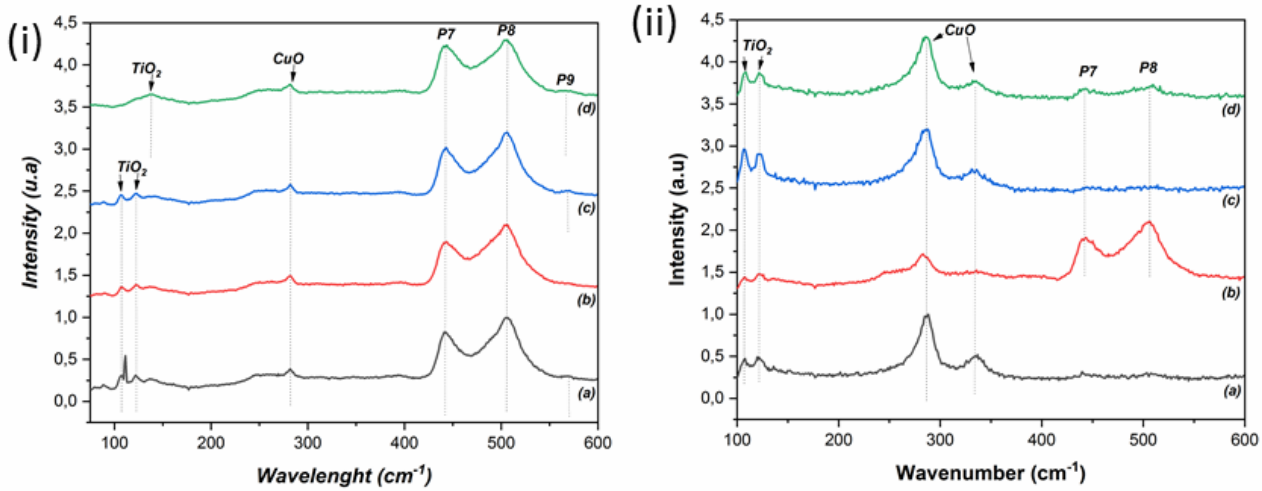

Figure 6 : Raman shifts on (i)-grains and (ii)-grain boundaries of (a) CCTO, (b) C1BN, (c) C3BN and (d) C6BN pellets.

Optical properties

Photoluminescence spectroscopy is used to study the efficiency of charge carrier trapping, migration and transfer. It is used in order to understand the recombinaition between electrons and holes in which a lower recombination rate induce a lower PL intensity. Figure 7a shows the PL spectra for CCTO and B,N doped CCTO measured with led excitation wavelenght (300 nm and 2 mW output power) with elimination of noise signals before measurements. The emission spectra have four significant peaks, centered at 390, 480, 700 and 800 nm. UV peak is related to band-band transitions with involvement of phonon [44]. UV emission can be related to band-band transitions or exciton emission [45]–[47]. Liu showed that intensity of excitonic emission depends on surface-to-volume ration of TiO_2 nanoparticles. The increase of the nanoparticle volume resulted in increase of defect emission. In the present work, the UV intensity increased for low concentration of BN doping and then decreased. The changes of UV PL can be related to change of lattice constants and lattice strain after BN doping [48], [49].

Emission, centered at 480 nm is related to self-trapped excitons and oxygen vacancies. Emission bands in NIR region correspond to surface defects [50]. Low intensities of Vis-NIR bands point to high ratio of surface recombination and charge separation.

The optical properties of materials were explored as well by UV-Vis diffuse reflectance spectroscopy and presented in Figure 7b. Since CCTO is a complex perovskite, it can present two band gap in direct and indirect transition [19] **(**Figure S2**)**.

The optical absorption spectra of all materials show the presence of two absorption, at around 450 nm and at 680 nm which are related to the hybridized valence band (VB) from Cu 3d−O 2p to conduction band (CB) with Ti−3d states (Figure 7b). In CCTO, the higher energy absorption edge arises due to direct transition from Cu *3d*- O *2p* hybridized valance band to the Ti-*3d* conduction band and the lower energy absorption is attributed as transition between valance band and unoccupied Cu *3d* band.

The absorption peak arround 575nm corresponding to 2.1 eV is refered to the transition between V_o (oxygen vacancies level) and VB and VC. There are slight shift of peaks due to the surface defects and the minor lattice expansion which is beneficial for photoelectroactivity under visible light exposition. The UV-Vis spectra shows a higher intensity for the composites material and we can notice a slight shift in the wavelengths indicating a change in the band-gap after the addition of Boron Nitride nanosheets to CCTO perovskite. The optical band gap Eg of the samples was determined by Kubelka-Munk remission function according to the following equation [51], [52]:

$$(F*hv)^2 = (hv - Eg)$$

Where F is the absorption coefficient, v is the light frequency and Eg is the direct transition band gap.

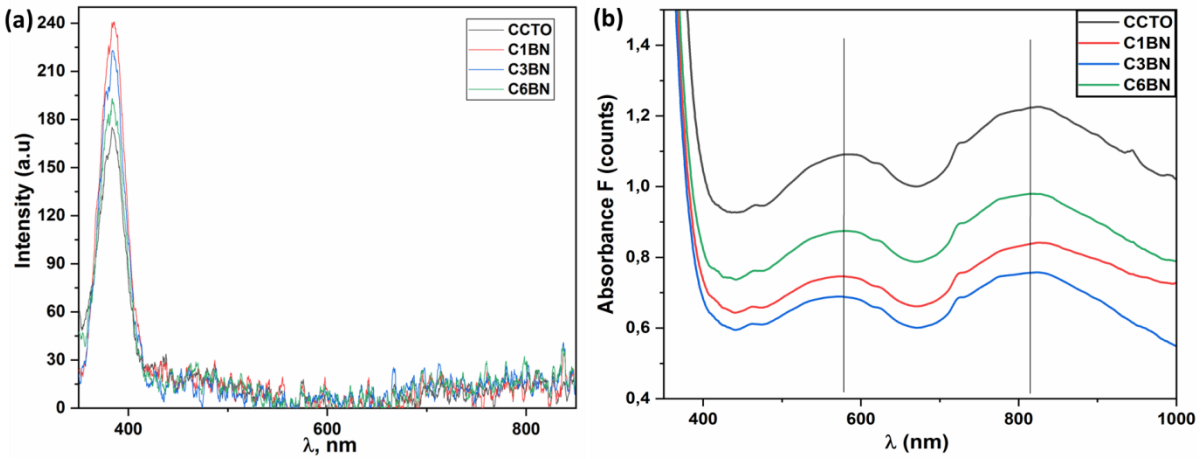

Figure 7 : **(a) Photoluminescence spectra and (b) UV-Vis diffuse reflectance spectroscopy, of CCTO, C1BN, C3BN, and C6 BN ceramics.**

The obtained Eg values for CCTO is 3.44 which is in a good correspondence with data, reported in [51] and 3.39, 3.38 and 3.37 eV for C1BN, C3BN and C6BN respectively, indicating a red shift in the band gap of the material with increasing the boron nitride nanosheets percentage. The band gap of composites could be affected by the presence of oxygen vacancies, and B and N ions in Ti-O bond linkage responsible. Thus the defect level between CB and VB is important to a better photo-electrocatalytic of the semi-conductor in visible light. B^{3+} and N^{3+} ions incorporated in TiO lattice can form a shallow level inside the band gap resulting in the decreasre of band gap energy and extend the spectral response to the visible region [44].

Electrochemical performances

Electrochemical properties of synthesized CCTO samples (CCTO, C1BN, C3BN and C6BN) were measured in dark and under visible exposition using three electrode systems in 1M KOH solution. All curves were recorded at a scan rate of 20 $mV.s^{-1}$ in the potential range of 0.25-1V (Figure 8a). Current density increases while increasing the percentage of nanofillers and after their exposure to visible light irradiation.

Capacitive characterization:

From cyclic voltammetry (CV) and a charge-discharge (CD) cycling, the capacitive behavior of a material can be estimated. The specific capacitance (SC) based on CV and CD cycling can be calculated as follows [53]:

i- $SC(CV)(F\ g\text{-}1) = {Q(c)}/{[scan\ rate * m(g)]}$

ii- $SC(CD)(F.g^{-1}) = {[i(A) * \Delta t(s)]}/{[\Delta E(V) * m(g)]}$

Where Q is the anodic charge, i is the discharge current in ampere, Δt is the discharge time in second corresponding to the voltage difference (ΔE) in volt, and m is the electrode mass in gram (active material).

CCTO activity is measured in ORR range in dark and under visible light exposition as shown in Figure 8a. The behavior of CCTO is different before and after irradiation. It seems inactive in

dark without any oxydation or reduction peaks. It can be seen that under visible light, a reduction peak appears at 0.47 V (vs AgCl/Ag) with no identifiable peak at anodic current. It can be explained by the high resistance of the material at high voltage. Under visible light exposition, the photogenareted current increases and CCTO showed a pseudocapacitive behavior.

It is clear that materials behavior change after adding nanofillers and under visible light irradiation, the larger integral area indicates the higher areal capacitance. The rectangular nature of CV curve for the composite C3BN (Figure 8b) measured in dark and under visible light showed symmetric anodic and cathodic halves without redox peaks thus indicates the ideal pseudocapacitive nature of material (high reversibility and high pulse charge discharge properties) [54]. The behavior of CCTO is different before and after irradiation; it can be seen that under visible light a reduction peak appears at 0.47 V vs. AgCl/Ag with no identifiable peak at anodic current. The distortion of CV curves shape indicates that the electrode does not store charge uniformly.

The behavior of the same samples was measured in OER range between 1 and 2.4 V vs. Ag/AgCl in 1M KOH using the three electrodes system. From figure 8c, it can be seen that electroactivity of CCTO change after adding 3% of BN nanosheets. A reduction peak appears and the cathodic current is generated. Under visible light, C3BN exhibit a larger reduction peak at slightly lower potential. The linear behavior of all samples at anodic potential (>1.4V) suggests that the electrodes could be oxidatively stable in this scanning potential range and that the resistance of the material at high potential becomes higher. This behavior is explained by many factor, one of them is the presence of CuO at grain boundaries. According to XRD and XPS results, Cu-defects on grain boundaries appeared after sintering and during cooling can act as acceptors, besides the n-type semiconductor grains [55]. It is well known that CuO is used as an active agent in electrochemical reaction, especially in their micro and nanoscale because they can generate an intracellular reactive oxygen species such as hydrogen peroxide [56]. The best behavior is given for C3BN with a pseudocapacitive behavior in dark and under exposure of visible light, because of the presence of more than one phase (TiB_2, B-O-Ti, and oxygen vacancies) known as semiconducting and good electronic transport agents comparable to metals or metal oxides [28], [57]. The higher photocurrent density was observed under the light illumination from LSV current in OER and ORR range (Figure 9a,b) for C3BN pellets which was attributed as light harvesting ability and

narrow band gap of the composite. The interband electron transition due to photon absorption during visible light irradiation results into the generation of photocurrent and four fold increase of current density. LSV and cyclic voltammetry showed that the C3BN can be used effectively as photocatalysts and photoelectrode materials. The onset in ORR range is at 0.5V.

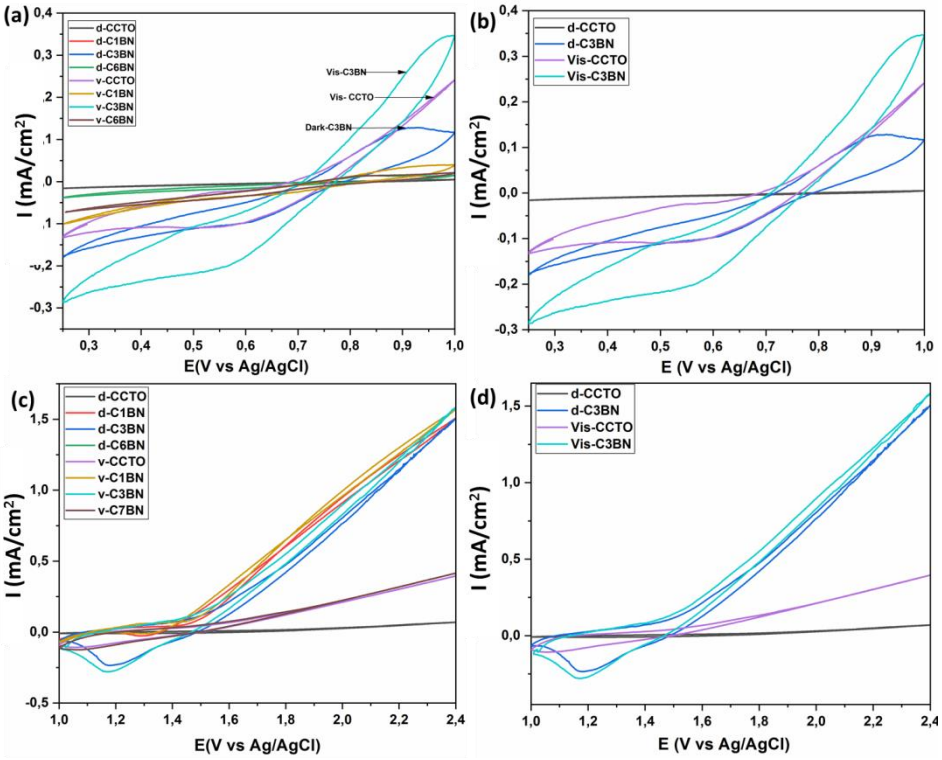

Figure 8: CV curves (a) CCTO, C1BN, C3BN, and C6 BN ceramics in dark and under visible light in ORR range. (b) CCTO and C3BN in dark and under visible light in ORR range. (c) CCTO, C1BN, C3BN, and C6 BN ceramics in dark and under visible light in OER range (In 1M KOH vs Ag/AgCl)

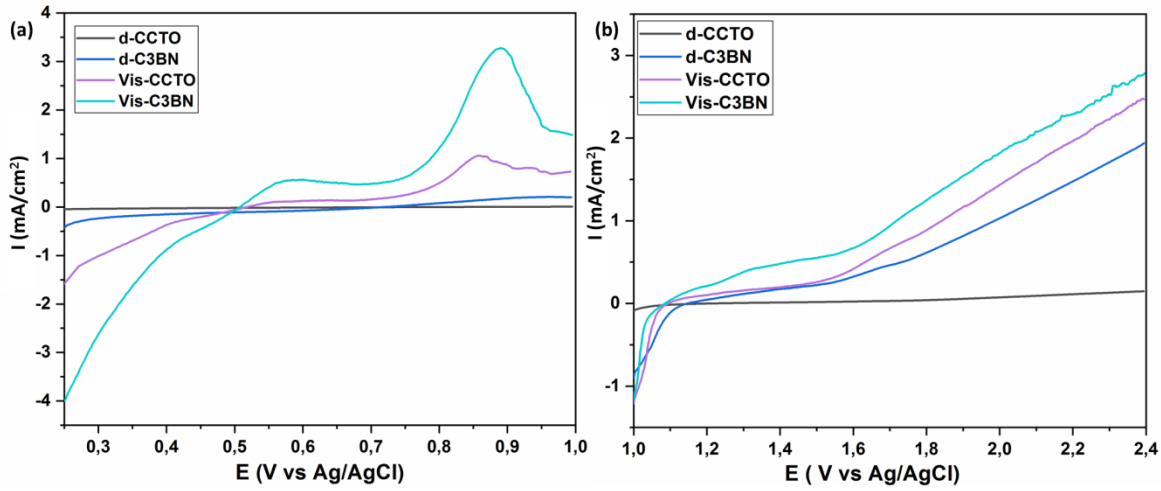

Figure 9: LSV curves of CCTO, C1BN, C3BN, and C6BN ceramics in dark and under visible light irradiation in 1M KOH vs Ag/AgCl in (a) ORR range and (b) OER rang

Electrochemical Impedance Spectroscopy

Electrochemical impedance spectroscopy (EIS) is used to evaluate the electrical conductivity and capacitive characteristics of electrode materials. Figure S3 (a,b,c) shows the Nyquist plots of our materials in the applied potential range of 0.4V-0.6V vs. Ag/AgCl under dark and visible light.

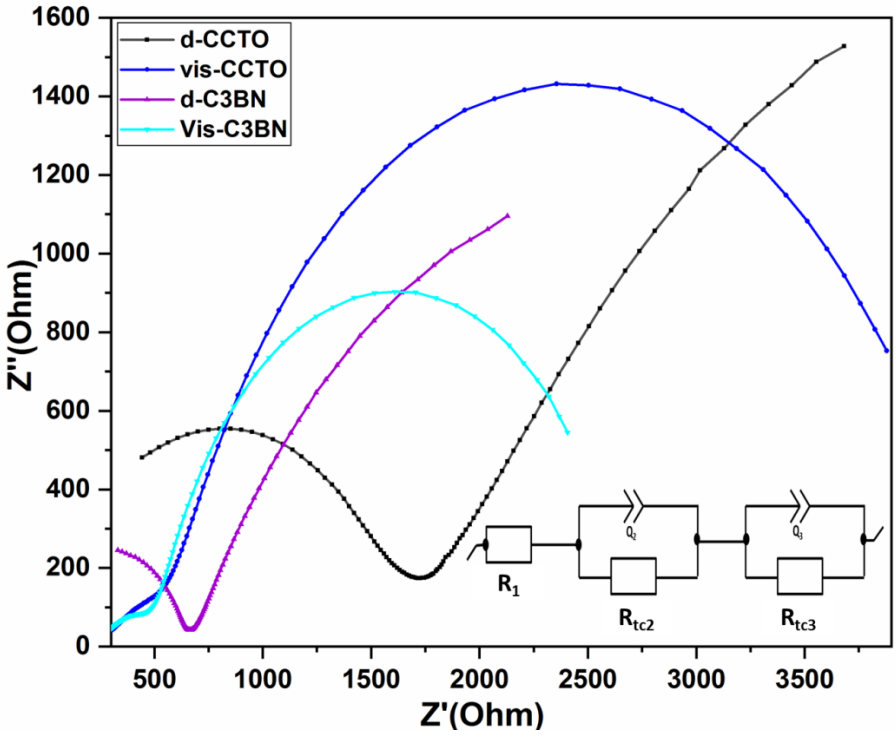

Figure 10 : The Nyquist plot of CCTO and C3BN ceramics in dark and under visible light irradiation at (a) 0.5V vs Ag/AgCl

As shown in Figure 10, all Nyquist plots showed a small semi-circle in high and medium frequencies and a large semi-circle in low frequency region but the arc diameter change for different material. The larger semi-circle is showed for pure CCTO, it can be seen that the resistance decreases after adding nanosheets and after their exposure to visible light irradiation For quantitative analysis, experimental data of impedance spectra have been fitted to the model depicted by the equivalent circuit shown in Figure 10. In the model of Figure 10, R_1 is the resistance of electrolyte (1M KOH solution). The parallel combination of the interfacial charge transfer resistance (R_2 and R_3 resistance of grains boundaries and grain respectively) and the constant phase element (CPE) is also included in this circuit. The CPE instead of a capacitor is taken in consideration for frequency dispersion. R_2 and R_3 values are mentioned in Table S2. The resistances decrease after adding BN nanosheets. This could be related to the formation of conducting CuO phases at grain boundaries and the presence of surface defects as oxygen vacancies due to the B-N codoped TiO_2 lattice. This finding indicates that the formation of Ti synergetic bond with N and B atoms produce more accessible active sites and multi charged electrons for electrochemical reactions [58], [59].

First step of oxygen reduction reaction takes place when the oxygen molecules are absorbed on the surface of the catalysts and it reduced into O^{2-}. The lowest resistance is given for C3BN under visible light which is in agreement with CV curves. The EIS analysis confirms that the C3BN under visible light has better charge transport properties which results into improved electrocatalytic activity during oxygen reduction reaction.

Under visible light exposition, CCTO behavior change and the current density start to increase. A reduction peak appear leading to the decrease of CCTO resistance. The infinite transmissive diffusion process start to increase at dark after adding BN nanosheets. Best behavior was recorded to C3BN under visible light as shown from CV curves in ORR range (Figure 8a), and the lowest resistance as shown from Nyquist plots, due to the increased adsorption of O^{2-} on the catalysts surface. The lowest charge transfer resistance results into higher production of the peroxide ion (HO^{2-}). The adsorption of HO^{2-} on the catalysts surface is the second step of the oxygen reduction reaction. As presented in Figure S4 (C3BN), the resistance increases while decreasing the applied potential because of the adsorbed

peroxide ion on the electrode surface. In the last step of oxygen reduction, the peroxide species are further reduced into H_2O. From equation (1) the capacitive current can be calculated using the parameters given by fitting Nyquist plots, whereas the capacitive current increase from $1.11*10^{-2}$ to $5.3*10^{-2}$ for CCTO in Dark and CCTO_3BN under exposure of visible light respectively.

Hydrogen Evolution

In order to study the photoelectrochemical activity for hydrogen production in presence of the elaborated ceramics CCTO and C3BN, measurements have been performed for two hours in a system of three electrodes, in which our elaborated ceramics were the anode electrode (on OER) and Platinum was the cathode electrode (on HER) in presence of reference electrode (Ag/AgCl) as shown in Figure 11. It can be observed that the rate of H_2 production on Pt surface under visible light increases after adding 3% of hexagonal BN nanosheets to CCTO. It can be observed that the rate of H_2 production under visible light increases after adding 3% of hexagonal BN nanosheets to CCTO. The hydrogen yield reached arround 8.1 µmol/h, which presents 16 times compared with CCTO. This enhancement could be related to the fact that C3BN resistivity decreases and that electrons transfer is more efficient between the impurities level between CB and VB under visible light irradiation, which is seen from EIS measurements. The average faradaic efficiency values were evaluated to be 73.3% and 82.9% for CCTO and C3BN respectively. The higher efficiency could be attributed to the higher photocurrent density seen from LV measurements.

To evaluate the durability of the C3BN sample, the hydrogen production by photoelectrochemical experiments was performed in four cycles where each cycle lasts for 2 h as shown in Figure 13. It can be seen that the production of hydrogen was linear and stable during these cycles

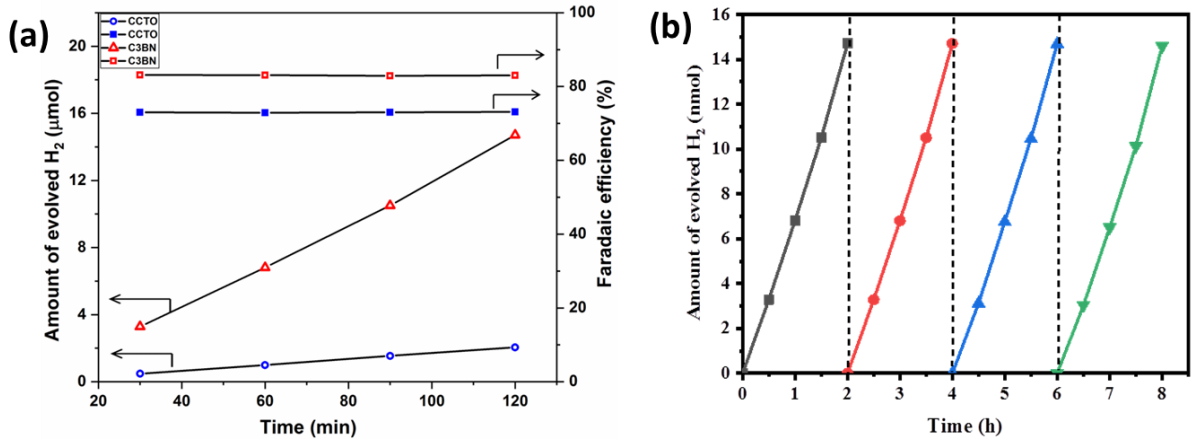

Figure 11 : (a) The faradaic efficiency and quantity of detected hydrogen derived from the CCTO (blue symbols) and C3BN (red symbols) and (b) Reusability of C3BN ceramics for photoelectrochemical H_2 production activity, under visible light.

Conclusion

Research investigations are focused to find an active photoelectrode under visible light irradiation in order to ameliorate the photoelectrochemical cell efficiency. In this study $CaCu_3Ti_4O_{12}$ ceramics with different amounts of hexagonal boron nitride nanosheets (1, 3, and 6%) were prepared. Using Reitveld refinement of XRD data, the formation of crystalline phase for all CCTO based materials with small amount of CuO as second phase is detected. The characteristic peaks of h-BN nanosheets are not detected due to the oxidation of h-BN at high temperature. SEM/EDX mapping and Raman spectroscopy showed the segregation of CuO phase on grain boundaries and that increases with increasing h-BN weight percentage in the composites. XPS spectra confirm the incorporation of bore (B) and nitrogen (N) into CCTO lattice. The B and N co-dopant CCTO enhances the partial reduction of Cu^{2+} and Ti^{4+} which is seen by the lattice expansion shown by XRD and the shift of peaks to lower binding energy by XPS, leading to create oxygen vacancy on the surface for charge compensation. The described microstructure of co-doped CCTO materials showed a red shift in band gap energy value detected by UV-Vis spectra. Furthermore, electrochemical measurement were performed in dark and under visible light exposure, they showed that adding h-BN nanosheets co-doped CCTO lattice with B and N and enhances the materials efficiency. The photocurrent generation is enhanced 16 times for CCTO with 3% of h-BN under visible light irradiation in comparison to CCTO. This activity is induced by the presence of new bond in CCTO lattice after the insertion of B and N elements (Ti-O-N and Ti-B-O) and the generated oxygen vacancy on the surface. The conductivity of the studied materials was measured using Electrochemical impedance spectroscopy. The measurements showed that the insertion of co-

doped elements and CuO segragation on grain boundaries enhance the electron conductivity on the interface between materials surface and the electrolyte. Hydrogen production measurements have been performed and shown that the rate of H_2 production under visible light increases after adding 3% of hexagonal BN nanosheets to CCTO. The hydrogen yield reached arround 8.1 μmol/h, which presents 16 times increase in comparison with CuO/CCTO.

References

[1] X. Tong *et al.*, "Engineering the Optoelectronic Properties of Colloidal Alloyed Copper Chalcogenide Quantum Dots for High-Efficiency Solar Energy Conversion," *Sol. RRL*, vol. 3, no. 10, p. 1900186, Oct. 2019.

[2] K.-H. Ye *et al.*, "Enhancing photoelectrochemical water splitting by combining work function tuning and heterojunction engineering," *Nat. Commun.*, vol. 10, no. 1, p. 3687, 2019.

[3] X. Tong *et al.*, "Optoelectronic Properties in Near-Infrared Colloidal Heterostructured Pyramidal 'Giant' Core/Shell Quantum Dots," *Adv. Sci.*, vol. 5, no. 8, p. 1800656, Aug. 2018.

[4] Y. Li, W. Liu, Z. Zhang, X. Du, L. Yu, and Y. Deng, "A self-powered electrolytic process for glucose to hydrogen conversion," *Commun. Chem.*, vol. 2, no. 1, p. 67, 2019.

[5] K.-Y. Show, Y. Yan, M. Ling, G. Ye, T. Li, and D.-J. Lee, "Hydrogen production from algal biomass – Advances, challenges and prospects," *Bioresour. Technol.*, vol. 257, pp. 290–300, 2018.

[6] N. Fakhimi, A. Dubini, O. Tavakoli, and D. González-Ballester, "Acetic acid is key for synergetic hydrogen production in Chlamydomonas-bacteria co-cultures," *Bioresour. Technol.*, vol. 289, p. 121648, 2019.

[7] A. Demirbaş, "Gaseous products from biomass by pyrolysis and gasification: effects of catalyst on hydrogen yield," *Energy Convers. Manag.*, vol. 43, no. 7, pp. 897–909, 2002.

[8] A. G. Tamirat, J. Rick, A. A. Dubale, W.-N. Su, and B.-J. Hwang, "Using hematite for photoelectrochemical water splitting: a review of current progress and challenges," *Nanoscale Horiz.*, vol. 1, no. 4, pp. 243–267, 2016.

[9] L. Hui *et al.*, "Overall water splitting by graphdiyne-exfoliated and -sandwiched

layered double-hydroxide nanosheet arrays," *Nat. Commun.*, vol. 9, no. 1, p. 5309, 2018.

[10] Y. Jiao, Y. Zheng, M. Jaroniec, and S. Z. Qiao, "Design of electrocatalysts for oxygen- and hydrogen-involving energy conversion reactions," *Chem. Soc. Rev.*, vol. 44, no. 8, pp. 2060–2086, 2015.

[11] D. T. Tran, H. T. Le, T. L. Luyen Doan, N. H. Kim, and J. H. Lee, "Pt nanodots monolayer modified mesoporous Cu@CuxO nanowires for improved overall water splitting reactivity," *Nano Energy*, vol. 59, pp. 216–228, 2019.

[12] N. Guijarro *et al.*, "Evaluating spinel ferrites MFe2O4 (M = Cu, Mg, Zn) as photoanodes for solar water oxidation: prospects and limitations," *Sustain. Energy Fuels*, vol. 2, no. 1, pp. 103–117, 2018.

[13] Y. Guo, Y. Fu, Y. Liu, and S. Shen, "Photoelectrochemical activity of ZnFe2O4 modified α-Fe2O3 nanorod array films," *RSC Adv.*, vol. 4, no. 70, pp. 36967–36972, 2014.

[14] J. Zhang, Z. Zhao, Z. Xia, and L. Dai, "A metal-free bifunctional electrocatalyst for oxygen reduction and oxygen evolution reactions," *Nat. Nanotechnol.*, vol. 10, p. 444, Apr. 2015.

[15] F. Cao, G. Oskam, G. J. Meyer, and P. C. Searson, "Electron Transport in Porous Nanocrystalline TiO2 Photoelectrochemical Cells," *J. Phys. Chem.*, vol. 100, no. 42, pp. 17021–17027, Jan. 1996.

[16] W. Li *et al.*, "WO3 Nanoflakes for Enhanced Photoelectrochemical Conversion," *ACS Nano*, vol. 8, no. 11, pp. 11770–11777, Nov. 2014.

[17] S. Sakthivel, M. Janczarek, and H. Kisch, "Visible Light Activity and Photoelectrochemical Properties of Nitrogen-Doped TiO2," *J. Phys. Chem. B*, vol. 108, no. 50, pp. 19384–19387, Dec. 2004.

[18] J. Su, L. Guo, N. Bao, and C. A. Grimes, "Nanostructured WO3/BiVO4 Heterojunction Films for Efficient Photoelectrochemical Water Splitting," *Nano Lett.*, vol. 11, no. 5, pp. 1928–1933, May 2011.

[19] D. C. Sinclair, T. B. Adams, F. D. Morrison, and A. R. West, "CaCu3Ti4O12: One-step internal barrier layer capacitor," *Appl. Phys. Lett.*, vol. 80, no. 12, pp. 2153–2155, Mar. 2002.

[20] J. H. Clark *et al.*, "Visible Light Photo-oxidation of Model Pollutants Using CaCu3Ti4O12: An Experimental and Theoretical Study of Optical Properties, Electronic

Structure, and Selectivity," *J. Am. Chem. Soc.*, vol. 133, no. 4, pp. 1016–1032, Feb. 2011.

[21] J.-W. Lee, G.-H. Lee, D.-J. Shin, J. Kim, S.-J. Jeong, and J.-H. Koh, "Ag-migration effects on the metastable phase in CaCu3Ti4O12 capacitors," *Sci. Rep.*, vol. 8, no. 1, p. 1392, 2018.

[22] H. S. Kushwaha, N. A. Madhar, B. Ilahi, P. Thomas, A. Halder, and R. Vaish, "Efficient Solar Energy Conversion Using CaCu3Ti4O12 Photoanode for Photocatalysis and Photoelectrocatalysis," *Sci. Rep.*, vol. 6, p. 18557, Jan. 2016.

[23] H. S. Kushwaha, A. Halder, P. Thomas, and R. Vaish, "CaCu3Ti4O12: A Bifunctional Perovskite Electrocatalyst for Oxygen Evolution and Reduction Reaction in Alkaline Medium," *Electrochim. Acta*, vol. 252, pp. 532–540, 2017.

[24] S. Maity, M. Samanta, A. Sen, and K. K. Chattopadhyay, "Investigation of electrochemical performances of ceramic oxide CaCu3Ti4O12 nanostructures," *J. Solid State Chem.*, vol. 269, pp. 600–607, 2019.

[25] M. Weber *et al.*, "Enhanced electrocatalytic performance triggered by atomically bridged boron nitride between palladium nanoparticles and carbon fibers in gas-diffusion electrodes," *Appl. Catal. B Environ.*, vol. 257, p. 117917, 2019.

[26] D. Gonzalez Ortiz, C. Pochat-Bohatier, J. Cambedouzou, M. Bechelany, and P. Miele, "Pickering emulsions stabilized with two-dimensional (2D) materials: A comparative study," *Colloids Surfaces A Physicochem. Eng. Asp.*, vol. 563, pp. 183–192, 2019.

[27] M. Bechelany, A. Brioude, S. Bernard, P. Stadelmann, D. Cornu, and P. Miele, "Boron nitride multiwall nanotubes decorated with BN nanosheets," *CrystEngComm*, vol. 13, no. 21, pp. 6526–6530, 2011.

[28] M. Nasr *et al.*, "High photodegradation and antibacterial activity of BN–Ag/TiO2 composite nanofibers under visible light," *New J. Chem.*, vol. 42, no. 2, pp. 1250–1259, 2018.

[29] M. Öner, A. A. Çöl, C. Pochat-Bohatier, and M. Bechelany, "Effect of incorporation of boron nitride nanoparticles on the oxygen barrier and thermal properties of poly(3-hydroxybutyrate-co-hydroxyvalerate)," *RSC Adv.*, vol. 6, no. 93, pp. 90973–90981, 2016.

[30] V. Thangaraj *et al.*, "Fluorescence Quenching of Sulfo-rhodamine Dye over Graphene Oxide and Boron Nitride Nanosheets," *Eur. J. Inorg. Chem.*, vol. 2016, no. 13-14, pp.

2125–2130, May 2016.

[31] J. Biscarat, M. Bechelany, C. Pochat-Bohatier, and P. Miele, “Graphene-like BN/gelatin nanobiocomposites for gas barrier applications,” *Nanoscale*, vol. 7, no. 2, pp. 613–618, 2015.

[32] Rodriguez-Carvajal, J. Recent Developments Of The Program FULLPROF, in commission on powder diffraction (IUCr), Newsletter 2001, 26, 12–19.

[33] R. Schmidt, S. Pandey, P. Fiorenza, and D. C. Sinclair, “Non-stoichiometry in ‘CaCu3Ti4O12’ (CCTO) ceramics,” *RSC Adv.*, vol. 3, no. 34, pp. 14580–14589, 2013.

[34] M. A. de la Rubia, J. J. Reinosa, P. Leret, J. J. Romero, J. de Frutos, and J. F. Fernández, “Experimental determination of the eutectic temperature in air of the CuO–TiO2 pseudobinary system,” *J. Eur. Ceram. Soc.*, vol. 32, no. 1, pp. 71–76, 2012.

[35] J. Boonlakhorn, P. Kidkhunthod, N. Chanlek, and P. Thongbai, “(Al3+, Nb5+) co–doped CaCu3Ti4O12: An extended approach for acceptor–donor heteroatomic substitutions to achieve high–performance giant–dielectric permittivity,” *J. Eur. Ceram. Soc.*, vol. 38, no. 1, pp. 137–143, Jan. 2018.

[36] B. Bajorowicz *et al.*, “4 - Application of metal oxide-based photocatalysis,” in *Metal Oxides*, A. B. T.-M. O.-B. P. Zaleska-Medynska, Ed. Elsevier, 2018, pp. 211–340.

[37] R. Hailili, Z.-Q. Wang, X.-Q. Gong, and C. Wang, “Octahedral-shaped perovskite CaCu3Ti4O12 with dual defects and coexposed {(001), (111)} facets for visible-light photocatalysis,” *Appl. Catal. B Environ.*, vol. 254, pp. 86–97, Oct. 2019.

[38] S. V Bobylev and I. A. Ovid’ko, “Stress-driven migration of deformation-distorted grain boundaries in nanomaterials,” *Acta Mater.*, vol. 88, pp. 260–270, 2015.

[39] D. Magnfält, A. Fillon, R. D. Boyd, U. Helmersson, K. Sarakinos, and G. Abadias, “Compressive intrinsic stress originates in the grain boundaries of dense refractory polycrystalline thin films,” *J. Appl. Phys.*, vol. 119, no. 5, p. 55305, Feb. 2016.

[40] T.-T. Fang and Y.-H. Wang, “Reassessment of copper and titanium valences and excess holes in oxygen 2p levels of CaCu3Ti4O12,” *J. Electrochem. Soc.*, vol. 158, no. 9, pp. G207–G210, 2011.

[41] Z. Liu *et al.*, “Ultrathin high-temperature oxidation-resistant coatings of hexagonal boron nitride,” *Nat. Commun.*, vol. 4, no. 1, p. 2541, 2013.

[42] S. Orrego, J. A. Cortés, R. A. C. Amoresi, A. Z. Simões, and M. A. Ramírez, “Photoluminescence behavior on Sr2+ modified CaCu3Ti4O12 based ceramics,”

Ceram. Int., vol. 44, no. 9, pp. 10781–10789, Jun. 2018.

[43] S. Rani, N. Ahlawat, K. M. Sangwan, R. Punia, and A. Kumar, "An approach for correlating electrically heterogeneous structure to enhanced dielectric properties of Sr and Zn co-substituted CaCu3Ti4O12 ceramics," *J. Alloys Compd.*, vol. 769, pp. 1102–1112, Nov. 2018.

[44] M. H. Reilly, "Temperature dependence of the short wavelength transmittance limit of vacuum ultraviolet window materials—II theoretical, including interpretations for U.V. spectra of SiO2, GeO2, and Al2O3," *J. Phys. Chem. Solids*, vol. 31, no. 5, pp. 1041–1056, 1970.

[45] L. Kernazhitsky *et al.*, "Room temperature photoluminescence of anatase and rutile TiO2 powders," *J. Lumin.*, vol. 146, pp. 199–204, 2014.

[46] S. Mathew *et al.*, "UV-Visible Photoluminescence of TiO2 Nanoparticles Prepared by Hydrothermal Method," *J. Fluoresc.*, vol. 22, no. 6, pp. 1563–1569, 2012.

[47] B. Liu, L. Wen, and X. Zhao, "The photoluminescence spectroscopic study of anatase TiO2 prepared by magnetron sputtering," *Mater. Chem. Phys.*, vol. 106, no. 2, pp. 350–353, 2007.

[48] M. Tsega and F. B. Dejene, "Influence of acidic pH on the formulation of TiO2 nanocrystalline powders with enhanced photoluminescence property," *Heliyon*, vol. 3, no. 2, p. e00246, 2017.

[49] M. Tsega and F. B. Dejene, "Tailoring luminescence properties of a sol–gel drivenTiO2 nanoparticles by ammonia treatment," *Mater. Res. Express*, vol. 4, no. 3, p. 35018, 2017.

[50] I. Iatsunskyi *et al.*, "Study on Structural, Mechanical, and Optical Properties of Al2O3–TiO2 Nanolaminates Prepared by Atomic Layer Deposition," *J. Phys. Chem. C*, vol. 119, no. 35, pp. 20591–20599, Sep. 2015.

[51] M. Ahmadipour, S. N. Ayub, M. F. Ain, and Z. A. Ahmad, "Structural, surface morphology and optical properties of sputter-coated CaCu3Ti4O12 thin film: Influence of RF magnetron sputtering power," *Mater. Sci. Semicond. Process.*, vol. 66, pp. 157–161, 2017.

[52] A. A. Felix, M. Spreitzer, D. Vengust, D. Suvorov, and M. O. Orlandi, "Probing the effects of oxygen-related defects on the optical and luminescence properties in CaCu3Ti4O12 ceramics," *J. Eur. Ceram. Soc.*, vol. 38, no. 15, pp. 5002–5006, Dec. 2018.

[53] T. Shinomiya, V. Gupta, and N. Miura, “Effects of electrochemical-deposition method and microstructure on the capacitive characteristics of nano-sized manganese oxide,” *Electrochim. Acta*, vol. 51, no. 21, pp. 4412–4419, 2006.

[54] C.-C. Hu and T.-W. Tsou, “Ideal capacitive behavior of hydrous manganese oxide prepared by anodic deposition,” *Electrochem. commun.*, vol. 4, no. 2, pp. 105–109, Feb. 2002.

[55] L.-T. Mei, H.-I. Hsiang, and T.-T. Fang, “Effect of Copper-Rich Secondary Phase at the Grain Boundaries on the Varistor Properties of CaCu3Ti4O12 Ceramics,” *J. Am. Ceram. Soc.*, vol. 91, no. 11, pp. 3735–3737, Nov. 2008.

[56] G. Zampardi *et al.*, “Electrochemical Behavior of Single CuO Nanoparticles: Implications for the Assessment of their Environmental Fate,” *Small*, vol. 14, no. 32, p. 1801765, Aug. 2018.

[57] F. Huang *et al.*, “Facile Synthesis, Growth Mechanism, and UV−Vis Spectroscopy of Novel Urchin-like TiO2/TiB2 Heterostructures,” *Cryst. Growth Des.*, vol. 9, no. 9, pp. 4017–4022, Sep. 2009.

[58] D. Hassen *et al.*, “Nitrogen-doped carbon-embedded TiO2 nanofibers as promising oxygen reduction reaction electrocatalysts,” *J. Power Sources*, vol. 330, pp. 292–303, Oct. 2016.

[59] K. Zhang, X. Wang, T. He, X. Guo, and Y. Feng, “Preparation and photocatalytic activity of B–N co-doped mesoporous TiO2,” *Powder Technol.*, vol. 253, pp. 608–613, Feb. 2014.